PNAS RESEARCH ARTICLE | ENGINEERING

# Comparison of copper and graphene-assembled films in 5G wireless communication and THz electromagnetic-interference shielding

Rongguo Song[a], Boyang Mao[b,c,1], Zhe Wang[a,d], Yueyue Hui[a], Ning Zhang[a], Ran Fang[a], Jingwei Zhang[a], Yuen Wu[e], Qi Ge[c], Kostya S. Novoselov[b,c,f,g,1], and Daping He[a,d,1]

Edited by John Rogers, Northwestern University, Evanston, IL; received June 7, 2022; accepted December 28, 2022

**Since first developed, the conducting materials in wireless communication and electromagnetic interference (EMI) shielding devices have been primarily made of metal-based structures. Here, we present a graphene-assembled film (GAF) that can be used to replace copper in such practical electronics. The GAF-based antennas present strong anticorrosive behavior. The GAF ultra-wideband antenna covers the frequency range of 3.7 GHz to 67 GHz with the bandwidth (BW) of 63.3 GHz, which exceed ~110% than the copper foil-based antenna. The GAF Fifth Generation (5G) antenna array features a wider BW and lower sidelobe level compared with that of copper antennas. EMI shielding effectiveness (SE) of GAF also outperforms copper, reaching up to 127 dB in the frequency range of 2.6 GHz to 0.32 THz, with a SE per unit thickness of 6,966 dB/mm. We also confirm that GAF metamaterials exhibit promising frequency selection characteristics and angular stability as flexible frequency selective surfaces.**

graphene-assembled film | 5G technology | flexible electronics | wireless communication | electromagnetic protection

## Significance

The concerns for consuming copper in electronics keep increasing because of its poor ability to couple with next generation devices. Here, working from tens of MHz to THz, we show a GAF featuring a combination of ultrahigh conductivity and durable flexibility that can be applied to wireless communication electronics and EMI shielding. Unlike previously reported graphene strucutres, the GAF can be directly used in commerical consumer electronics for advanced functions. The GAF devices show some specific and/or better performance, for example: flexibility, strong anticorrosion behavior, wider bandwidth, high shielding effectiveness, and so on. Our research demonstrates that the graphene macroscopic film can be used as a fully functional and sustainable alternative in current and next generation devices.

The matured development of 5G and emerging Sixth Generation (6G) wireless communication electronics (WCE) has the potential to revolutionize many applications such as healthcare (1), fitness monitoring (2), wearable communication (3, 4), Internet of Things (5), e-skins (6, 7), and so on, making our lives more convenient, safe, and productive. To efficiently transport electrical signals and electromagnetic waves at multicommunication bands, the 5G and 6G networks require more antennas, much larger bandwidths (BWs), and a higher density of base stations than that of previous generations. In particular, high data transmission rate and low fault tolerance require a wireless communication system to possess narrow radiation beam and low radiation sidelobe to reduce signal crosstalk. As a result, the demand for WCE will skyrocket in the approaching years: for example, the number of global 5G base stations is expected to reach 65 million by 2025 (8). Together with the explosive growth of WCE devices, particularly mobile terminals, serious issues of electromagnetic interference (EMI) have also arisen, which can lead to signal loss, data misinterpretation, and even system failure (9, 10). The increased electromagnetic pollution can also be hazardous to human health (11).

In general, the electrical conducting component in WCE devices and effective EMI shielding materials require high electrical conductivity as well as high electron mobility (12). Metals have such characteristics (with electrical conductivity of over $10^7$ S/m and electron mobility of 10 to 50 $cm^2/V\,s$) (13). So previous WCE devices and EMI shielding materials have conventionally been made from metal-based structures for decades (14, 15). However, with the growing demands for being flexible and highly integratable, lightweight, smaller in size, easy-to-fabricate, and operating at higher frequency communication bands (from dozens of GHz up to THz), the metal material-based structures are beginning to show less ability to cope with next generation WCE and EMI shielding requirements (16). Moreover, with the increasing number of electronic products, corrosion has an increasing impact on electronics. Corrosion of the antenna and other components may lead to malfunctions or even failures of electronic devices. In addition, besides the pollutants and $CO_2$ emission generated during metal mining and manufacturing processes (17, 18), sustainable development in the next generation consumer electronics becoming essential due to the growing environmental impacts associated with the electronic waste (e-waste).

Metal-free WCE devices and EMI shielding material are, however, challenging to make, since it is hard to have a material simultaneously matching the high electrical conductivity and presenting good mechanical stability. In recent years, carbon-based electronics, especially the possibility of exploiting graphene to assemble macroscopic structures has been

Author contributions: R.S., B.M., and D.H. designed research; Z.W., Y.H., N.Z., and R.F. performed research; R.S., Z.W., J.Z., Y.W., and Q.G. analyzed data; and R.S., B.M., K.S.N., and D.H. wrote the paper.

The authors declare no competing interest.

This article is a PNAS Direct Submission.



[1]To whom correspondence may be addressed. Email: maoboyang@gmail.com, kostya@manchester.ac.uk, or hedaping@whut.edu.cn.

This article contains supporting information online at https://www.pnas.org/lookup/suppl/doi:10.1073/pnas.2209807120/-/DCSupplemental.

Published February 22, 2023.

demonstrated as a feasible approach to reach the target (19–21). Previous research demonstrated that graphene can be directly grown (like chemical vapor deposition), implanted or printed on a substrate to form a composite/hybrid structure (22, 23). However, the conducting graphene layer in these structures typically has limited thickness or low conductivity, which results in high surface resistance and poor device performance (24, 25). Recent breakthroughs in the reduction of graphene oxide (GO) (26) and exfoliation of pristine grapheme (27) have demonstrated that graphene-assembled structures can reach electrical conductivities of up to $10^5$ S/m (28–30), and that such techniques can be applied in WCE (31–33). Such electrical conductivity, however, is still two orders of magnitude lower than that of metal-based materials. Meanwhile, MXene, as a unique family of two-dimensional (2D) transition metal carbides and/or nitrides, can be used as an alternative material to achieve this goal. MXene has a high electrical conductivity (around $10^5$ S/m) and can provide effective electromagnetic shielding performance with low thicknesses (9, 34), as well as be applied in WCE (35). However, MXene are still metal-containing materials and are easily oxidized (unsuitable for long-term use) and difficult to produce in large quantities (36), which limits their application in real-world commercial products. Furthermore, so far, novel 2D material-based WCE devices and EMI shielding materials have only been demonstrated as concept validations with simple functions, no practical and advanced electronics have been designed or systematically compared with metal-based, especially copper, commercial devices in terms of robustness and device performance, etc. yet (37–40).

Here, we report a graphene-assembled film (GAF) with a conductivity of $2.58 \times 10^6$ S/m and applied it in next generation WCE and EMI shielding materials to directly compare with copper-based devices. After 200,000 bending tests (with a bending radius of 1.5 mm), the GAF film can retain its high flexibility and conductivity with no structural damages. To investigate GAF's capabilities in 5G technology and flexible electronics, we first demonstrated its stable performance in 5G WCE as flexible coplanar waveguide transmission lines and 1/4 wavelength resonators under various twisting conditions. GAF-based dipole antennas have a −39 dB reflection coefficient and a high gain of 1.89 dBi, which is comparable to copper-based antennas. Furthermore, the GAF antenna is highly anticorrosive compared with copper: after 2 wk of salt spray treatment, it retains its $|S_{11}|$ and gain, whereas copper-based antennas lose over 4.68 dBi for their gain. We investigated an integrated wearable 5G communication system based on all-GAF flexible electronics, including a flexible wearable antenna, filter, and a 2 × 2 antenna array. A working mechanism for a graphene-based ultra-wideband (UWB) antenna (with BW of 63.3 GHz) and a 5G antenna array (with 140 antenna elements and high gain of 24.23 dBi) are also proposed. The working BW of the GAF UWB antenna is increased by 116.8% and, the radiation sidelobe is reduced by more than 5.9 dB compared with a copper antenna. For a 5G antenna array, the beam width and sidelobe level of the E-plane and H-plane, respectively, are 8°, −21.76 dB and 6°, −24.94 dB, which is much better than the copper antenna array (8°, −18.84 dB and 6°, −19.03 dB). GAF further is investigated over a frequency range of 2.6 GHz to 0.32 THz for EMI shielding performance. GAF has an electromagnetic shielding effectiveness (EMI SE) of up to 127 dB in the low-frequency band (2.6 GHz to 40 GHz) and more than 80 dB, surpassing copper's SE value, in the high-frequency band (40 GHz to 0.32 THz) and with a maximum EMI SE per unit thickness of 6,966 dB/mm, which outperforms copper-based devices. Two flexible frequency selective surface (FSS) based on GAF are designed, operating at 3.5 GHz and 60 GHz, respectively, and exhibiting good frequency selection characteristics and angular stability. Thus, our research demonstrates GAF's full potential as a sustainable alternative or even a better material to replace copper in multiband 5G communication electronics and EMI shielding for next-generation WCE.

## Results

**GAF Fabrication and Characterization.** To achieve graphene-based films with a high electrical conductivity, we introduce extremely large flake size graphene oxides (LGO) as the film's building precursor to reduce the contribution of contact resistance. The detailed fabrication procedures are described in *Materials and Methods*. With commercially standard equipment, GAF can be manufactured in a viable and scale manner, *SI Appendix*, Figs. S1 and S2 (41). Fig. 1*A* is a transmission electron microscope (TEM) image that presents a typical LGO sheet with a lateral size of 108 μm. The detailed structures of GO flake under higher resolution TEM display as defects-containing morphology (*SI Appendix*, Fig. S3 *A–F*), originating from oxygen-containing functional groups with no lattice structures on the surface. As demonstrated by elemental mapping images in *SI Appendix*, Fig. S3 *G–J*, the O element is distributed evenly on the surface of GO flake, implying that oxygen-containing functional groups has covered the initial honeycomb structure composed of carbon atoms. In the corresponding size distributions curve from optical microscope measurement and Raman mapping images, Fig. 1*B* and *SI Appendix*, Fig. S4*A*, the average LGO lateral size is around 110 μm, which is significantly larger than any previously reported study (42, 43). To compare, films made from typical size GO flakes, *SI Appendix*, Fig. S4*C*, have also been fabricated as a control experiment and been tested accordingly. GAF was manufactured by an optimized compression and a secondary high-temperature (2,850 °C) graphitization process. The Raman, Diffraction of X-rays (XRD), and X-ray Photoelectron Spectroscopy (XPS) spectra (*SI Appendix*, Fig. S4 *D–K*) of GAFs after annealing from 1,150 to 2,850°C during the process confirm the elimination of oxygen and recrystallization. The XRD (Fig. 1*C*) and Raman spectroscopy (Fig. 1*C* and *SI Appendix*, Fig. S4*L*) confirm GAF's highly graphitized and almost no defects structure. Based on Raman measurement, a large crystallite size $L_a$ = 1,967.95 nm in the GAF is also confirmed according to Eq. 1 (44).

$$L_a(nm) = \left(2.4 \times 10^{-10}\right) \lambda_l^4 \left(\frac{I_D}{I_G}\right)^{-1}. \quad [1]$$

Small-angle X-ray scattering (SAXS) patterns of GAF, inserted in Fig. 1*D*, show a prismatic scattering pattern indicating GAF with highly aligned layered structure. In contrast, for a typical flake size GO-assembled film (TGF), *SI Appendix*, Fig. S4*M*, no such pattern is identified (45). *SI Appendix*, Fig. S4*N* is the top view GAF SEM image, microfolds are uniformly distributed on the GAF surface. As shown in *SI Appendix*, Fig. S4*O*, the cross-section SEM images of the GAF characterize a thin film with thickness of ~19 ± 0.5 μm. This thickness is similar to a commercial copper foil applied in consumer electronic devices. Although metal materials, like gold (Au), silver (Ag), copper (Cu), aluminim (Al), and iron (Fe), has higher electrical conductivity, the apparent density of GAF (1.92 g/cm$^3$) is significantly lower, shown in *SI Appendix*, Fig. S5 *A* and *B*. In addition, the mechanical measurements of GAF are tested, as shown in the *SI Appendix*, Fig. S5*C*. The tensile strength of GAF is 59.51 MPa with the longitudinal strain of 4.42%. The resistance change of

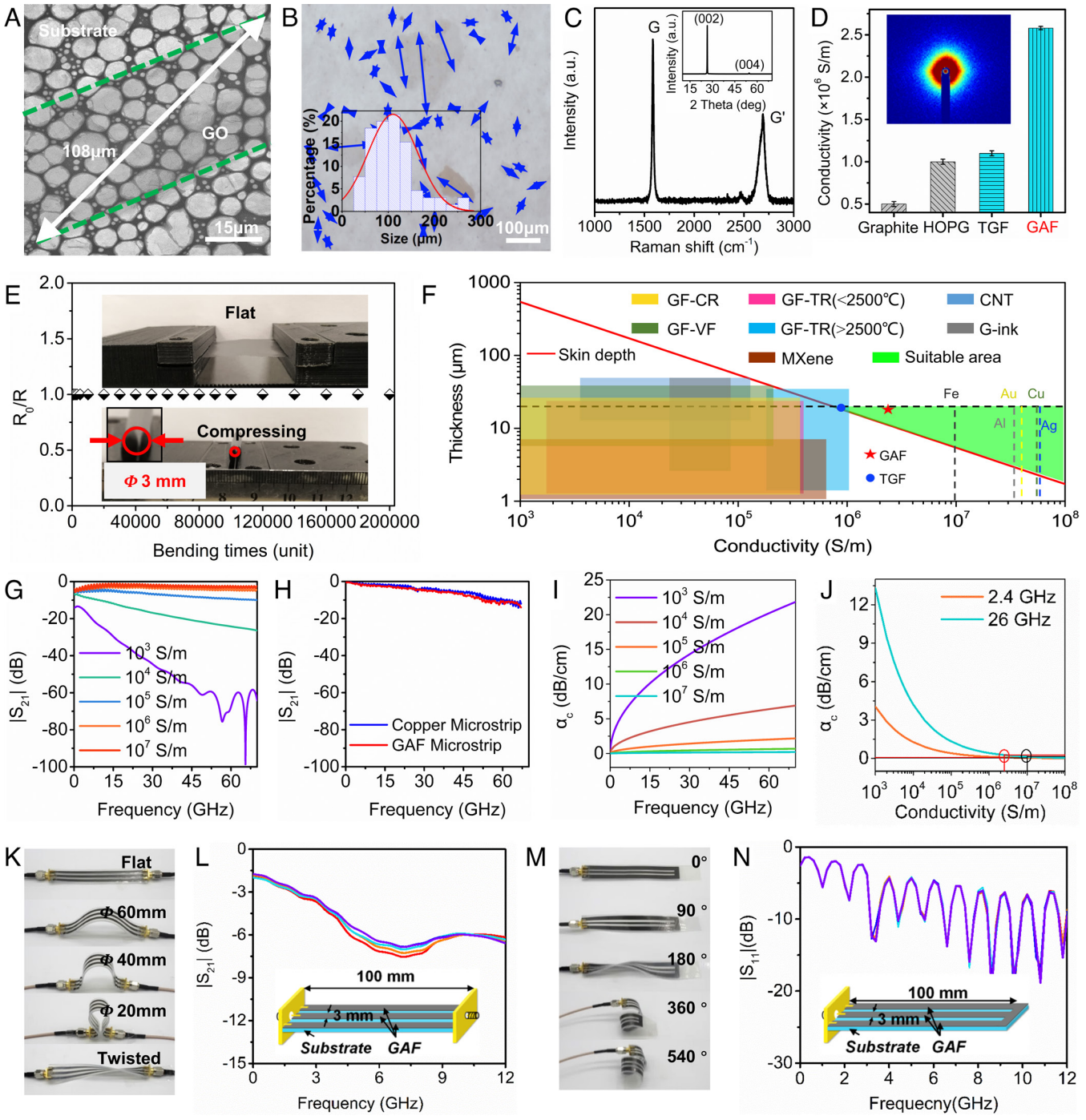


**Fig. 1.** GAF characterization. (*A*) TEM image of a typical large-sized GO sheet with a lateral size of 108 μm (The green line represents the edge of the GO sheet). (*B*) Optical microscope image of LGO sheets preparing *via* drop casting LGO solution on $SiO_2$ surface. the inserted is a statistic study corresponding LGO size distributions (The blue arrows indicate the size of GO sheet). (*C*) GAF's XRD pattern and Raman spectrum. (*D*) A summary of conductivities of GAF, graphite, Highly Oriented Pyrolytic Graphite (HOPG), and Typicalflake Size GO Assembled Film (TGF), the insert is SAXS pattern. (*E*) Resistance change of GAF with 200,000 repeating bending test to proof durable flexibility and stability (The red circle shows the magnification of the bending part). (*F*) Skin depth at 860 MHz associated with electrical conductivity and the conductive layer thickness of the GF prepared by chemical reduction, vacuum filtration, thermal reduction GO film and other methods, graphene ink, Carbon Nanotubes (CNT), and MXene. (*G* and *H*) The simulated (*G*) and measured (*H*) transmission coefficient of MTL. (*I* and *J*) The conductor loss under different frequency (*I*) and conductivity (*J*). (*K*) Flexible GAF FCPW TL being bent with diameters of 60 mm, 40 mm, 20 mm and twisted 180°. (*L*) Transmission coefficient of the FCPW TL in different states between 10 MHz and 40-GHz frequency band (red-flat, orange-60 mm, wathet-40 mm, blue-20 mm, and purple-twisted). (*M*) Flexible GAF λ/4 short-circuited resonator at diffident twisting condition: untwisted, twisted 90°, 180°, 360°, and 540°. (*N*) Resonator's reflection coefficient results at different twisting condition, between 10 MHz and 12 GHz frequency band (red-flat, orange-90°, wathet-180°, blue-360°, and purple-540°).

GAF is very small (less than 0.1 Ω), which is within the strain bearing range, as shown in *SI Appendix*, Fig. S5*D*. In Fig. 1*E* and Movie S1, we demonstrate that GAF can retain its ultrahigh conductivity even after 200,000 bending cycles test with a bending radius of 1.5 mm (*SI Appendix*, Table S1). The SEM images show the durability of GAF that can endure a zigzag folding without any breakage (*SI Appendix*, Fig. S5 *G* and *H*). A similar test was performed on a commercial copper foil with the thickness of 20 μm; the copper foil broke after only 12-folds (*SI Appendix*, Fig. S5*I*).

The electrical conductivity of all samples is measured by a four-probe method (*SI Appendix*, Fig. S6 *A* and *B* and Movie S2). In *SI Appendix*, Fig. S6*E*, the electrical conductivity of GAF and TGF fabricated under different conditions are characterized. The conductivity of GAF is 2.58 ± 0.06 × $10^6$ S/m, which is five times higher than that of a graphite film (5 × $10^5$ S/m) and about two times higher than HOPG (1 × $10^6$ S/m) and TGF (9 × $10^5$ S/m). In *SI Appendix*, Fig. S6 *C* and *D*, the electron transfer pathway between GAF and TGF is proposed as the mechanism for this ultrahigh electrical conductivity (46). At high frequency, the skin depth effect cannot be negligible. To better integrate in 5G WCE electronics, the thickness of conducting material in the device always is demanded to be around 20 μm or below (47). The skin depth $\delta$ can be calculated by the following Eq. 2.

$$\delta = \frac{1}{\sqrt{\pi f \mu \sigma}}, \quad [2]$$

where $f$ is the frequency, $\mu$ is the permeability and $\sigma$ is the conductivity of conductive material. For nonmagnetic conducting materials, $\mu$ is taken as $4\pi \times 10^{-7}$ N/$A^2$. Taking the Radio Frequency Identification (RFID) communication frequency band (860 MHz) specified in Electronic Product Code (EPC) Gen2 standard as an example, to reduce the resistance loss, the thickness of conductive material should be greater than skin depth. Regarding this, in Fig. 1*F*, a selective area which requires materials having electrical conductivity higher than 0.75 × $10^6$ S/m is identified. For nonmetal materials, it can be found that among all novel developed materials, only graphene films (GFs) made by high-temperature (over 2,500 °C) annealing can meet these requirements (*SI Appendix*, Fig. S6*F* and Tables S2 and S3).

To investigate the conductivity of GAF in radio frequency (RF) current and directly compare with copper, two microstrip transmission line (MTL)-based GAF and copper are designed and measured, as shown in *SI Appendix*, Fig. S6*G*. The transmission coefficient of MTL under different conductivity is shown in Fig. 1*G*. It is obvious that the transmission loss of MTL increases with the decrease in conductivity. When the conductivity exceeds $10^6$ S/m, the MTL transmission loss varies very little, demonstrating the minimal conductivity needed of the novel material used in the construction of RF and microwave devices. The transmission coefficient of GAF MTL and copper MTL are measured through the vector network analyzer (Keysight N5247A), as shown in Fig. 1*H*, which proves that the conductive mechanism model of GAF and metal is the same at high-frequency. In addition, the relationship between conductivity and conductor loss is shown in Fig. 1*I*. When the conductivity reaches more than $10^6$ S/m, the correlation between conductor loss and conductivity becomes not particularly strong. Even in the millimeter wave band, the loss is less than 1 dB/cm. As shown in Fig. 1*J*, the conductor loss difference between GAF and copper is 0.06 dB/cm and 0.2 dB/cm at 2.4 GHz and 26 GHz, respectively. In particular, the GAF with the conductivity of 2.58 × $10^6$ S/m has the conductor losses of 0.08 dB/cm, 0.27 dB/cm at 2.4 GHz and 26 GHz, respectively.

To verify the excellent flexibility of GAF electronics, a flexible coplanar waveguide transmission line (FCPW TL) and a λ/4 short-circuited resonator based on a silica gel film (*SI Appendix*, Fig. S6*H*) are first designed and fabricated. As shown in Fig. 1 *K* and *L*, FCPW TL's transmission characteristics of the being bent and twisted at different conditions are investigated between the 10 MHz and 12 GHz frequency band. It is found that bending and twisting has negligible effects on the transmission coefficient ($|S_{21}|$) of GAF transmission line. Fig. 1 *M* and *N* illustrate the reflection coefficient ($|S_{11}|$, between 10 MHz and 12 GHz band) of GAF λ/4 short-circuit resonator in the original state and different twist states. Like GAF flexible transmission line, the twist does not change the resonator's performance.

**GAF as a Dipole Antenna and Its Highly Anticorrosion Properties.** A GAF dipole antenna is used in this study as an example to compare with metal antennas in terms of device performance and corrosion resistance, which is a continuing concern in next-generation WCE working at higher frequencies and operating powers. Fig. 2*A* is the digital photo of the GAF dipole antenna and the copper foil-based antenna in the same pattern (design details in *SI Appendix*, *Experimental Section* and *SI Appendix*, Fig. S7*A*). The measured gain of antennas in the 0.7 GHz to 1.0 GHz frequency band and at 865 MHz are shown in Fig. 2 *B* and *C*, respectively. The GAF antenna has a gain of 1.89 dBi, which is comparable to the copper antenna of 1.94 dBi. This gain is much higher than that of the graphite antenna (1.05 dBi), HOPG antenna (1.39 dBi), and TGF antenna (1.35 dBi). Fig. 2 *D* and *E* present the three-dimensional (3D) and 2D radiation patterns of the GAF antenna at 865 MHz, also indicating a matching performance with the copper antenna. The measurement environments for the antennas are exhibited in Fig. 2 *F* and *G*. In Fig. 2*H*, the GAF dipole antenna exhibits the highest gain of any graphene-based dipole antenna reported in the literature (48–52). In *SI Appendix*, Fig. S7*B*, the E-field distribution simulation results of the graphene dipole antenna in different phases indicate the current on the dipole arm is sinusoidally distributed.

The salt spray treatment is applied to the GAF and copper antennas to investigate their corrosion resistance, *SI Appendix*, Fig. S7*C* and Fig. 2 *I* and *J* are the digital photos of the GAF antenna and copper antenna after 1-wk and 2-wk salt spray: the copper antenna is rusted and then broken after the test, but the exterior of the GAF antenna is unaffected. Fig. 2*K* illustrates the simulated and measured reflection coefficient $|S_{11}|$ at resonant frequencies of 865 MHz of the initial GAF antenna and after the salt spray treatments. The −10 dB BW of the GAF antenna is from 790 MHz to 980 MHz, which covers the RFID communication frequency band. After salt spray treatment, the GAF's $|S_{11}|$ does not change. However, the $|S_{11}|$ of the copper antenna becomes only −6.25 dB at 865 MHz after 2 wk of salt spray, Fig. 2 *L* and *M* present the measured gain at 865 MHz of GAF and copper antennas during the test, the gain of the GAF antenna is unchanged, but the copper antenna has a significantly lower gain of −2.74 dBi after 2 wk of salt spray. This test confirms that, unlike metal-based materials, because graphene is naturally more anticorrosive, no additional anticorrosion coating is required in the GAF WCE to protect it from corrosion, which significantly simplifies manufacturing process, reduces materials' weight, and production cost.

**Wearable Communication System and 5G Millimeter Wave Antenna with GAF.** In this work, we confirm that GAF antennas can be used to directly replace metal-based antennas in commercial sub-6-GHz electronic devices, like mobile phone and drone, without losing functionality, as shown in Fig. 3 *A*–*F* and *SI Appendix*, Fig. S8 *A* and *B* and Movies S3 and S4. To demonstrate GAF are capable of fabricating flexible Sub-6-GHz WCE, we build an integrated terminal and base mobile communication system with all GAF-based WCE, including a flexible GAF wearable antenna, 2 × 2 GAF antenna array, and GAF filter, as shown in *SI Appendix*, Fig. S8 *C*–*F*. The radiation patterns of the GAF antenna and antenna array recorded for every 10° of rotation in microwave anechoic chamber, Fig. 3*G*. In *SI Appendix*, Fig. S8 *G*–*I*, a communication system integrated with all above GAF electronics is demonstrated. The gain and

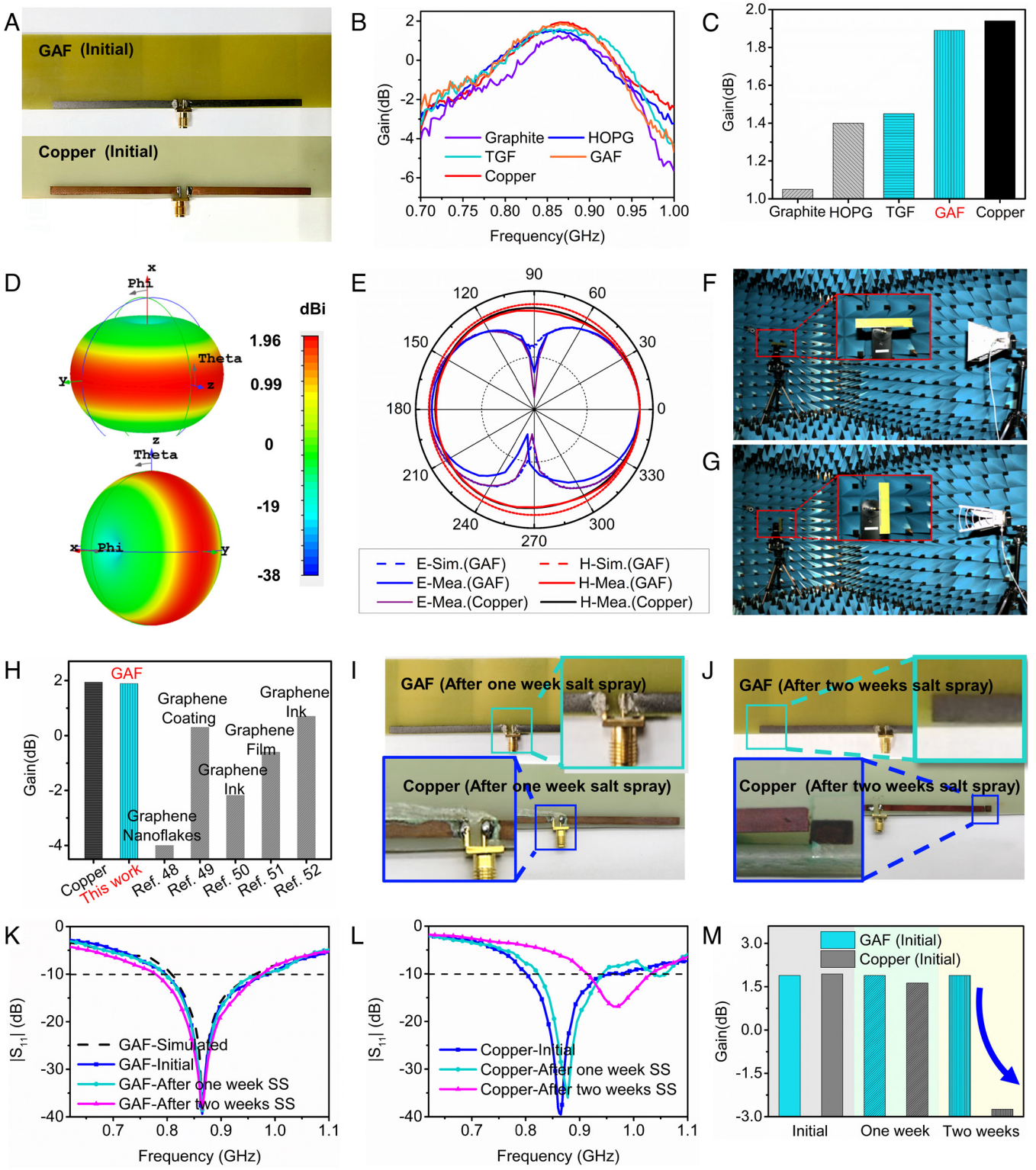


**Fig. 2.** GAF as a dipole antenna and its anticorrosion performance. (*A*) Digital photos of GAF and copper dipole antennas, (*B*) The measured gain of different material- based antennas in BW. (*C*) The gain of different material-based antennas at 865 MHz. (*D*) 3D radiation pattern simulation of GAF antenna. (*E*) Radiation patterns at E-plane and H-plane of GAF and copper antennas. (*F* and *G*) Measurement environments of radiation pattern at E-plane and H-plane, respectively. (*H*) Comparison of the dipole antenna gain in references with the results in this work. (*I* and *J*) Digital photo of GAF and copper dipole antennas after 1-wk and 2-wk salt spray. (*K*) Measured and simulated $|S_{11}|$ of GAF antenna, initial, after 1-wk and 2-wk salt spray. (*L*) Measured $|S_{11}|$ of copper antenna, initial, after 1-wk, and 2-wk salt spray. (*M*) The measured gain of GAF and copper antennas at 865 MHz with initial, after 1-wk, and 2-wk salt spray.

transmission coefficient of the flexible 5G GAF antenna and antenna array are measured, as shown in Fig. 3*H*. The gain of the two antennas reaches the maximum at the resonant frequency of 2.45 GHz, which is consistent with the measured $|S_{21}|$ (as in Fig. 3*H*, blue line). The measured results show that the GAF 5G WCE communication system can function reliably, and that the flexible 5G GAF antennas and transmission line are capable to fit and work on the human body to transmit signals.

Millimeter wave WCE, with the advantages of high directivity, small in size, high resolution, rich spectrum resources, and high

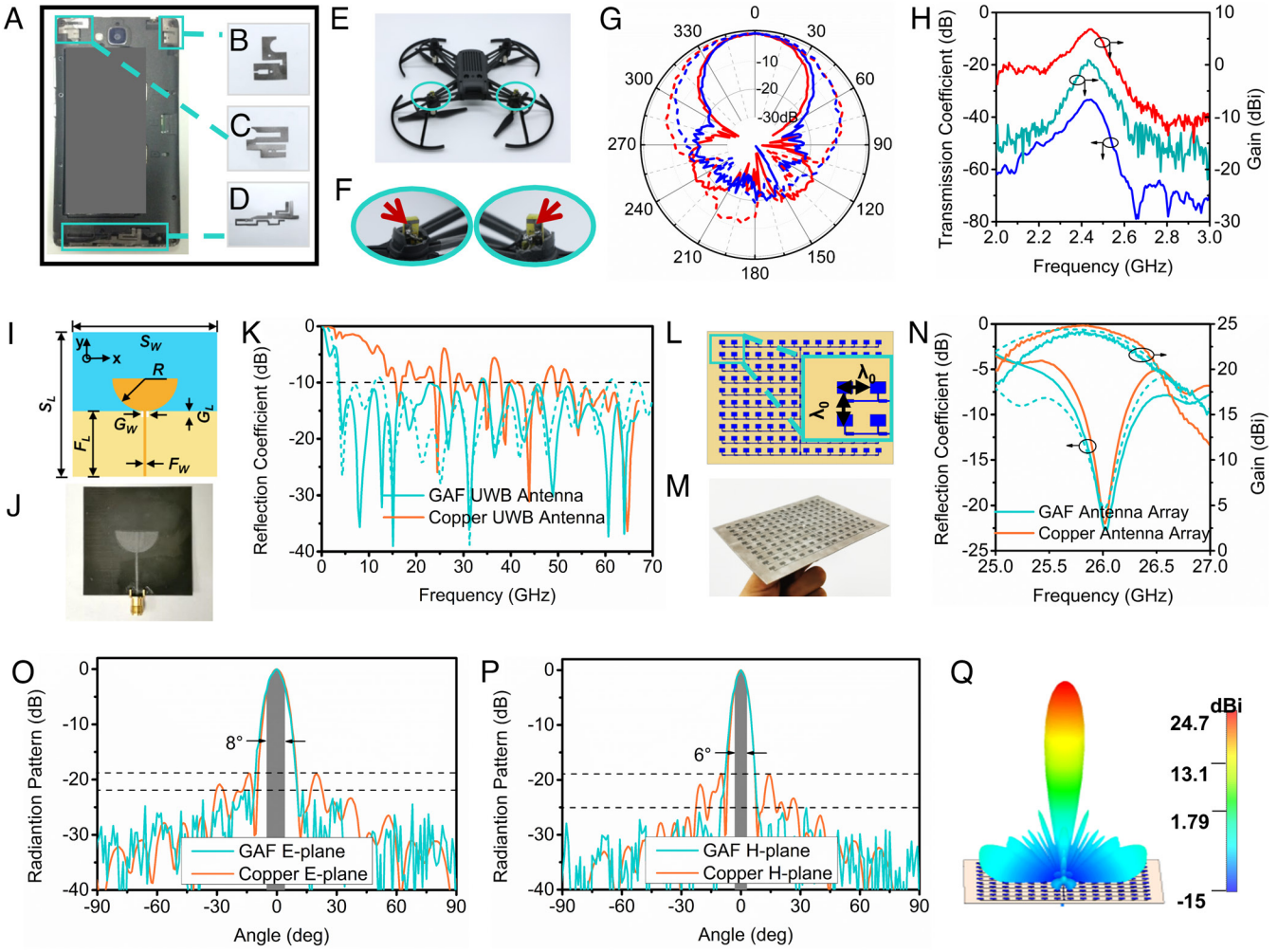


**Fig. 3.** GAF applied in Sub-6GHz wireless communication system and millimeter wave antenna. (*A*) Digital photo of mobile phone with GAF antennas. Digital photo of zoomed GAF mobile phone antennas: (*B*) Bluetooth antenna, (*C*) WiFi antenna, and (*D*) main communication antenna. (*E*) Digital photos of drone with GAF antennas. (*F*) Digital photo of zoomed GAF drone antennas. (*G*) The measured radiation patterns of the GAF wearable antenna and antenna array, the dashed and solid lines are the radiation patterns of the wearable antenna and the antenna array, respectively, the red line is E-plane, and the blue line is H-plane. (*H*) Measured transmission coefficient (blue line), gain of the GAF antenna array (red line) and wearable antenna (green line). (*I*) Structure of the GAF UWB antenna, overall size of UWB, $S_L = S_W = 50$ mm; $R = 10$ mm, $F_L = 20$ mm, $F_W = 0.8$ mm, $G_L = 0.7$ mm, $G_W = 1$ mm. (*J*) Digital photo of the GAF UWB antenna. (*K*) Measured (solid line) and simulated (dashed line) $|S_{11}|$ of the UWB antenna. (*L*) Schematic diagram of the GAF millimeter wave antenna array with the element spacing of $3/4\lambda$. (*M*) Digital photo of the GAF millimeter 5G antenna array with 140 elements. (*N*) Measured (solid line) and simulated (dashed line) reflection coefficient and gain of the GAF and copper 5G millimeter wave antenna array. (*O* and *P*) Measured E-plane and H-plane radiation patterns and (*Q*) the simulated 3D radiation patterns of the GAF and copper 5G millimeter wave antenna array.

information security, is an essential technology for the 5G mobile communication (53). To investigate GAF's abilities in millimeter wave 5G WCE, GAF-based 5G UWB antenna and 5G antenna array are studied. Fig. 3*I* illustrates the geometry of the proposed 5G UWB antenna. Fig. 3*J* and *SI Appendix*, Fig. S9*A* present the digital photograph of the proposed GAF-based UWB antenna and copper foil-based UWB antenna with the same structure. The measured −10 dB BW of the GAF UWB antenna covers the frequency range of 3.7 GHz to 67 GHz with the BW of 63.3 GHz (Fig. 3*K*), which is better than the copper antenna of 29.9 GHz. Because the GAF antenna has a lower quality factor ($Q$) value (negative correlation with conductivity) than that of the copper antenna with the same design pattern, resulting in a wider BW of the UWB antenna (BW ($|S_{11}|$<−10dB) $\approx \frac{1}{\sqrt{2}Q} \times 100\%$), it is believed that reducing conductivity of the conductor material in the device can be an effective way to increase antenna BW (54). Although the test frequency is up to 67 GHz, the actual impedance BW of the 5G UWB antenna is much wider. To gain insight into the radiation characteristics, we simulated the surface current distribution of the UWB antenna at 6 GHz, 10 GHz, 20 GHz, and 40 GHz. As shown in *SI Appendix*, Fig. S9*D*, current distribution demonstrates that the UWB antenna is working in its fundamental resonance mode at low-frequency band and in higher resonance mode at high-frequency band. A GAF 5G millimeter wave antenna array with the geometrical dimensions of 135 mm × 95 mm × 0.54 mm is fabricated, shown in Fig. 3 *L* and *M*. For comparation, the copper antenna array is fabricated, as shown in *SI Appendix*, Fig. S9*E*. The GAF 5G antenna array has 140 antenna elements (14 × 10), which accords with the Chebyshev current distribution. Fig. 3*N* illustrates the simulated and measured $|S_{11}|$ and gain from 25 GHz to 27 GHz. The GAF 5G antenna array operates at 26 GHz with a batter $|S_{11}|$ of −22.54 dB than copper antenna. The measured highest gain is 24.23 dBi, which matches with the simulated results and is comparable for the copper antenna array of 24.83 dBi. Fig. 3 *O* and *P* and *SI Appendix*, Fig. S9*F* depict the measured E-plane and H-plane radiation patterns. Due to the anisotropy of GAF, the antenna array has a sidelobe performance below −20 dB in E-plane and H-plane: the beam width and sidelobe level of the E-plane and

H-plane, respectively, are 8°, −21.76 dB, and 6°, −24.94 dB, which is much better than the copper antenna array: 8°, −18.84 dB, and 6°, −19.03 dB. The larger the difference in energy distribution between elements, the lower the radiation sidelobe of the array antenna (55). The energy is mostly concentrated on the transmission line before entering the antenna radiator. Because of its relatively poor conductivity, the GAF loses electromagnetic energy in the transmission line. The GAF antenna element located distant from the center has a long transmission distance and a high loss, which increases the difference in the energy distribution ratio, resulting in improved radiation sidelobe performance. The simulated 3D radiation patterns of the GAF 5G antenna array at 26 GHz are shown in Fig. 3*Q*, which also confirms the excellent sidelobe performance. Maintaining the similar gain (24.23 dBi) as a copper antenna (24.83 dBi), the lower conductivity of the graphene antenna results in better impedance BW and radiation sidelobe performance.

**GAF for EMI Shielding.** The EMI shielding performance of GAF in the frequency range of microwave band, millimeter wave band, and terahertz (THz) band is explored. First, the EMI SE at the frequency range of 2.6 GHz to 40 GHz is simulated and tested by the rectangular waveguide method, *SI Appendix*, Fig. S10 *A* and *B* and Fig. 4 *A*–*C* show the EMI SE of the GAF and commercial copper foils. The thickness of EMI SE produced from commercial copper foils (we tested thicknesses of 10 μm and 50 μm) has little effect on their EMI performance and presents an EMI SE of around 100 dB in the 2.6 GHz to 40-GHz frequency band. This is due to the fact that copper fully reflects electromagnetic waves, and the absorption effect is negligible. Due to the high conductivity, GAF exhibits ultra-high EMI SE. Additionally, because of its natural laminate structure, which causes absorption and multiple internal reflections (9), increasing the thickness of GAF can improve the EMI SE. The proposed GAF's EMI shielding mechanism is in *SI Appendix*, Fig. S10*C*. GAF's EMI SE with a thickness of 15 μm is greater than 80 dB and can achieve 90 to 100 dB above 6 GHz. When the thickness increases to 50 μm, the EMI SE of GAF rises to around 110 to 120 dB, especially at 13.5 GHz, where it reaches up to 127.3 dB. When the frequency exceeds 26 GHz, the GAF with a thickness of 15 μm exhibits the same EMI SE as a copper foil with a thickness of 50 μm. Furthermore, we use the free space method (*SI Appendix*, Fig. S10*D*) to evaluate GAF's EMI shielding performance over the frequency ranges of 40 GHz to 67 GHz, 75 GHz to 110 GHz, and 0.22 THz to 0.325 THz. As shown in

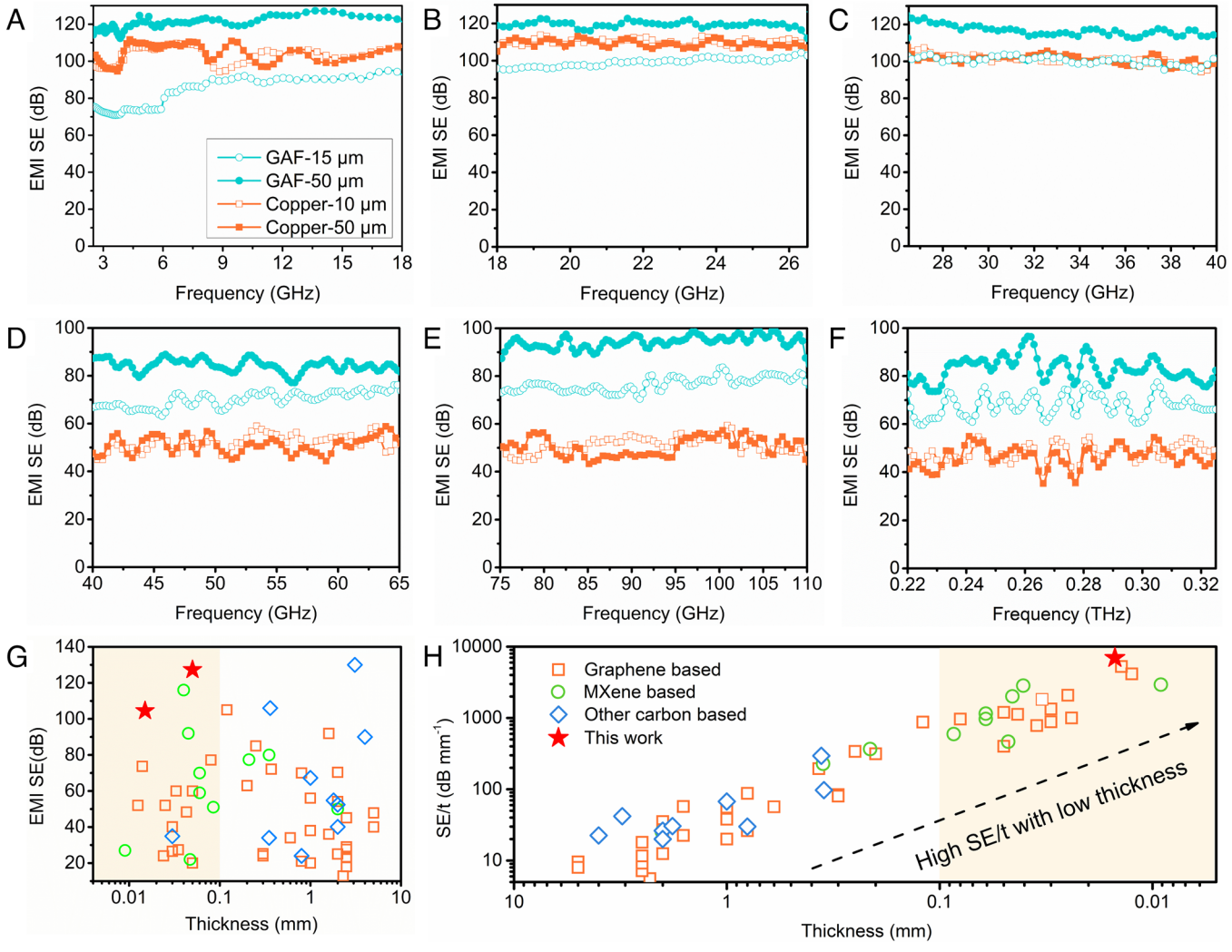


**Fig. 4.** GAF applied in EMI protection. (*A*–*F*) In the frequency range of 2.6 GHz to 0.32 THz, EMI SE of GAF with 15-μm and 50-μm thicknesses and copper with 10-μm and 50-μm thicknesses (With same legend), (*A*) 2.6 to 18 GHz (rectangular waveguide method), (*B*) 18 to 26.5 GHz (rectangular waveguide method), (*C*) 26.5 to 40 GHz (rectangular waveguide method), (*D*) 40 to 67 GHz (free space method), (*E*) 75 to 110 GHz (free space method), and (*F*) 0.22 to 0.3235 THz (free space method). (*G* and *H*) a comparison of SE and SE/t in references with the results in this work (the best results for the frequency bands given in the literature) (With same legend).

Fig. 4 *D–F*, GAF outperforms copper foil in terms of EMI shielding as frequency increases. The EMI SE of the GAF with a thickness of 15 μm and 50 μm is around 60 to 80 dB and 80 to 100 dB, respectively, which is higher than the 40 to 60 dB of the copper foil. The multilayer stacking structure of GAF has well multiple reflection and absorption ability for electromagnetic energy. We compared the recently reported EMI shielding performance of graphene-based and other materials, as shown in Fig. 4*G*. GAF is the electromagnetic shielding material that is closest to the ideal area, with the highest SE in the same thickness and the thinnest thickness in the same SE. Due to the importance of thickness to EMI shielding materials, SMI SE per unit thickness (SE/t) is used to characterize the EMI performance. Among other graphene structures, carbon nanotubes (CNT), carbon fibers, and MXene, GAF has the highest SE/t (6,966 dB/mm), as shown and compared in Fig. 4*H*.

**GAF Applied in FSS at Sub-6 GHz and Millimeter Wave Frequencies.** In addition to complete electromagnetic shielding, selective shielding of the electromagnetic field is also important in many cases to ensure the normal transmission of other frequency bands. As a member of metamaterials, FSS is formed by periodic arrangement of structural units, which can selectively absorb, reflect, and transmit electromagnetic waves (56), and thus is an effective way to realize frequency selection. To further explore the electromagnetic protection performance of GAF, we developed two transparent, flexible FSS that work in Sub-6 GHz and millimeter wave bands, respectively. Due to the higher requirement in flexibility and durability, the flexible FSS is hard to be produced by copper-based structure. First, a miniaturized flexible FSS based on GAF that works at 3.5 GHz is designed, *SI Appendix*, Fig. S11 *A* and *B*. The GAF FSS is with 12 × 12 periodic elements, fabricating by a high-precision laser engraving. The structure dimensions are 192 mm × 192 mm × 0.075 mm, as shown in Fig. 5*A*. The equivalent circuit diagram of the GAF FSS element is shown in *SI Appendix*, Fig. S11*C*, with the optimized parameter values shown in *SI Appendix*, Fig. S11 *D–F* and Table S5. GAF FSS is translucent and has a very low areal density of 0.0087 g/cm$^2$. GAF FSS is very flexible and can conform to curved surfaces (*SI Appendix*, Fig. S11*G*). Because of the presence of the bending line, the edge of the periodic element structure has a strong parasitic capacitance, as shown in *SI Appendix*, Fig. S11*H*, which can miniaturize the FSS. A high parasitic capacitance can also assist FSS maintain its angular stability. The transmission coefficient results of the periodic element are shown in *SI Appendix*, Fig. S11*I*. The FSS has a resonance frequency of 3.5 GHz, agreeing with the simulation results. In Fig. 5*B*, the E-field distribution can be used to investigate the working mechanism of FSS. It is clear that the FSS resonates at 3.5 GHz and generates large induced current, preventing electromagnetic waves from passing through the FSS. The measured transmission coefficient and shielding efficiency of GAF FSS under normal incidence of electromagnetic wave is shown in *SI Appendix*, Fig. S11*J*. *SI Appendix*, Fig. S10*K* is the measuring environment. In the 3.38 to 3.91 GHz frequency band, the transmission coefficient of GAF FSS is less than −10 dB, which means that FSS can shield more than 90% of electromagnetic waves. In particular, GAF FSS can shield 99.4% of electromagnetic waves at 3.5 GHz. Outside of this frequency band, electromagnetic waves can pass GAF FSS in a large proportion, proving that GAF FSS has good frequency selection characteristics. Fig. 5*C* are the spectrum curve of GAF FSS at different incident angles of electromagnetic waves, the transmission coefficient and working BW of GAF FSS remain essentially constant in the 0 to 25° range, indicating that GAF FSS has high angular stability. The measurement environment of GAF FSS in microwave anechoic chamber is show in *SI Appendix*, Fig. S11 *K* and *L*.

We also designed low-profile and UWB flexible millimeter wave FSS with a thickness of 0.138λ. The element structure of millimeter wave FSS is illustrated in *SI Appendix*, Fig. S12 *A* and *B*. The digital photos shown in Fig. 5*D* and *SI Appendix*, Fig. S12*C* demonstrate the FSS's flexibility. The FSS has the physical

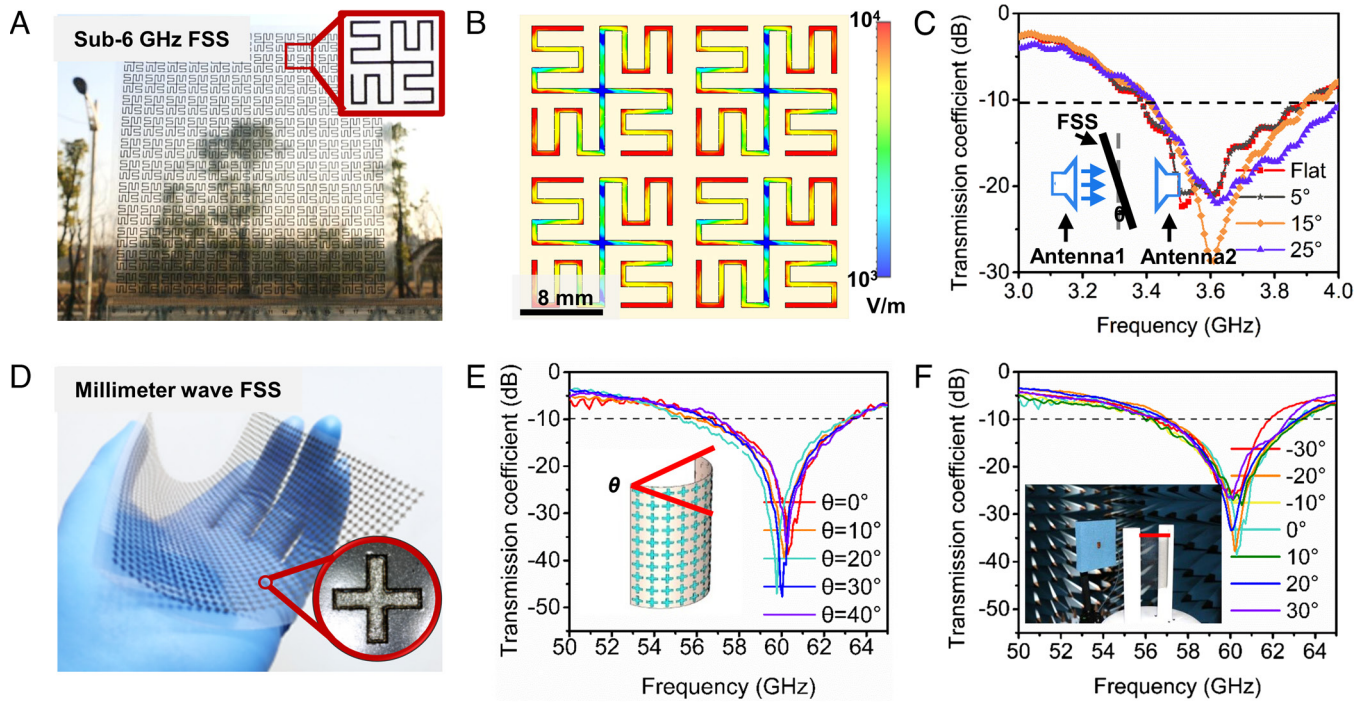


**Fig. 5.** GAF-based FSS. (*A*) The digital photo of Sub-6 GHz translucent GAF FSS, with 12 × 12 elements (The red rectangle shows the enlargement of FSS element). (*B*) E-field distribution of GAF FSS at 3.5 GHz (The color bar represents the amplitude of the E-field intensity). (*C*) The transmission coefficient of GAF FSS in incident obliquely of electromagnetic wave. (*D*) The digital photos of millimeter wave translucent GAF FSS with 40 × 40 elements (The red circle shows the magnification of the FSS element). (*E* and *F*) The transmission coefficient of GAF FSS in different bending states and incident obliquely of the electromagnetic wave.

dimensions of 125 mm × 125 mm × 0.065 mm implanting with 1,600 elements. *SI Appendix*, Fig. S12*D* illustrates the simulated transmission coefficient. GAF millimeter wave FSS covers a wide −10-dB BW of 8.16 GHz between 55.76 GHz and 63.92 GHz. *SI Appendix*, Fig. S12*E* is the surface current distribution of the GAF millimeter wave FSS at 60 GHz. It can be seen that the FSS resonates at 60 GHz and generates a strong induced current, hindering the passage of electromagnetic waves at 60 GHz. *SI Appendix*, Fig. S12*F* shows the measured transmission coefficient and shielding efficiency of GAF millimeter wave FSS under normal incidence of electromagnetic wave. The GAF FSS can shield 99.9% of electromagnetic waves at 60 GHz. Different bending states of GAF FSS and incident angles of electromagnetic waves can be achieved by varying the distance between two brackets and rotating the disc. As shown in Fig. 5*E*, the frequency selection performance of GAF FSS remains stable within a bending angle changing between 0° and 40°. Fig. 5*F* illustrates that GAF FSS maintains good frequency selection performance in the range of electromagnetic waves ± 30° incident angle.

## Discussion

Here, we demonstrate the advances of a lightweight, flexible, mechanically ultra-durable, highly chemically stable, and ultrahigh conductive GAF structures that can be applied in 5G multiband WCE and electromagnetic protection to directly compare and overcome some major issues with copper-based electronics. These GAF-based 5G electronics can be designed into a variety of sophisticated patterns and integrated into communication systems to achieve a wide range of advanced functions across the entire microwave communication frequency band. GAF has also demonstrated excellent electromagnetic shielding performance in the microwave and terahertz frequency bands, and it can be designed and fabricated into metamaterials to achieve selective electromagnetic wave shielding. Our research demonstrates that the highly conductive GF can be used as an alternative fully functional and sustainable material in RF fields, which can support current and next-generation flexible electronics, WCE, and EMI shielding applications in a more efficient and sustainable approach.

## Materials and Methods

**GAF Fabrication.** Two major approaches have been utilized to achieve high electrical conductivity of graphene-based laminates. First, we maximized the size of graphene crystallites, which allowed us to reduce the contribution of contact resistance. Second, we introduced secondary annealing process and special assembly technique, which allows highly laminated, defect-free assembly of such graphene crystallites into continuous films. First, GO was prepared via the modified Hummers method. The extremely LGO was separated and collected, and used as the film fabrication precursors. The LGO was separated from GO suspension (3 wt. %) after seven times repeating centrifugation (the bottom 30% GO are collected each time). An LGO lateral size statistical study is carried out by optical microscope: LGO with the lateral size >75 μm accounts for 74% and 54% of the LGO are >100 μm. The typical flake size graphene oxide (TGO) was used as it was synthesized and applied as a control experiment. The LGO-assembled film was prepared through premetered roll transfer coating of LGO hydrogel on a self-released substrate such as polyethylene terephthalate (PET) films. Subsequently, the LGO hydrogel on substrate was heated (70 to 80 °C) for drying. Thereafter, a soft, dark brown free-standing and paper-like GO film (LGO film) could be easily peeled off from the PET substrate. In this step, the anisotropic liquid crystalline behavior of LGO hydrogel can lead to a prealigned orientation structure after force-directed rolling transfer. This highly ordered laminate can be converted into a pristine GF in meters long scale via a high-temperature graphitization process. The LGO film was thermally annealed at 1,300 °C for 2 h and 2,850 °C for 1 h in Ar atmosphere between two graphite plates for reduction and graphitic crystallization. The giant crystalline graphitic domain size in a GAF is formed by the coalescence of neighboring reduced LGO sheets (57). GFs are fully graphitized after primary high-temperature annealing, allowing dangling-bond-free graphene nanosheets to tile on each other with broad-area plane-to-plane contacts. A rolling compression with the pressure of 300 MPa was further introduced to obtain the final GAF. The following rolling compression contributes to eliminate interlayer gaps and contact resistance, also leads to an excellent flexibility. Followed by the rolling compression, a secondary high-temperature annealing process at 2,850 °C in Ar atmosphere was carried out to further remove the structural damage during the rolling process to increase the electrical conductivity (58). TGF was obtained with the same method but from the TGO.

**Data, Materials, and Software Availability.** All study data are included in the article and/or *SI Appendix*.

**ACKNOWLEDGMENTS.** This work was financed by 2018 National Key R&D Program of China 257, the National Natural Science Foundation of China (Grant No.: 51672204, 51701146), the Fundamental Research Funds for the Central Universities (Wuhan University of Technology (WUT): 2020IB005, 205209016 and 2019IB017).

Author affiliations: [a]Hubei Engineering Research Center of Radio-Frequency (RF)-Microwave Technology and Application, Wuhan University of Technology, Wuhan 430070, China; [b]National Graphene Institute, University of Manchester, Manchester M13 9PL, UK; [c]Chongqing Two-Dimensional (2D) Materials Institute, Chongqing 400714, China; [d]State Key Laboratory of Silicate Materials for Architectures, Wuhan University of Technology, Wuhan 430070, China; [e]School of Chemistry and Materials Science, Collaborative Innovation Center of Chemistry for Energy Materials (iChEM), the Chinese Academy of Sciences (CAS) Center for Excellence in Nanoscience, University of Science and Technology of China, Hefei National Laboratory for Physical Sciences at the Microscale, Hefei 230026, China; [f]Department of Materials Science and Engineering, National University of Singapore, Singapore 117575, Singapore; and [g]Centre for Advanced Two-Dimensional (2D) Materials, National University of Singapore, Singapore 117546, Singapore

1. J. Kim, A. S. Campbell, B. E. de Ávila, J. Wang, Wearable biosensors for healthcare monitoring. *Nat. Biotechnol.* **37**, 389–406 (2019).
2. D. Das, S. Maity, B. Chatterjee, S. Sen, Enabling covert body area network using electro-quasistatic human body communication. *Sci. Rep. Uk* **9**, 4160 (2019).
3. M. Bariya, H. Y. Y. Nyein, A. Javey, Wearable sweat sensors. *Nat. Electron.* **1**, 160–171 (2018).
4. J. Kim *et al.*, Wearable smart sensor systems integrated on soft contact lenses for wireless ocular diagnostics. *Nat. Commun.* **8**, 14997 (2017).
5. Z. Ma *et al.*, High-reliability and low-latency wireless communication for internet of things: Challenges, fundamentals, and enabling technologies. *IEEE Int. Things J.* **6**, 7946–7970 (2019).
6. N. Li *et al.*, Large-scale flexible and transparent electronics based on monolayer molybdenum disulfide field-effect transistors. *Nat. Electron.* **3**, 711–717 (2020).
7. B. Wang *et al.*, Flexible and stretchable metal oxide nanofiber networks for multimodal and monolithically integrated wearable electronics. *Nat. Commun.* **11**, 2405 (2020).
8. C. Lin, S. Han, S. Bian, Energy-efficient 5g for a greener future. *Nat. Electron.* **3**, 182–184 (2020).
9. F. Shahzad *et al.*, Electromagnetic interference shielding with 2d transition metal carbides (MXenes). *Sci. (Am. Assoc. Adv. Sci)* **353**, 1137–1140 (2016).
10. Z. Wang *et al.*, Ultrahigh conductive copper/large flake size graphene heterostructure thin-film with remarkable electromagnetic interference shielding effectiveness. *Small* **14**, 1704332 (2018).
11. W. Cao *et al.*, Binary strengthening and toughening of MXene/cellulose nanofiber composite paper with nacre-inspired structure and superior electromagnetic interference shielding properties. *ACS Nano* **12**, 4583–4593 (2018).
12. T. R. Arabi, A. T. Murphy, T. K. Sarkar, R. F. Harrington, A. R. Djordjevic, On the modeling of conductor and substrate losses in multiconductor, multidielectric transmission line systems. *IEEE T. Microw. Theory* **39**, 1090–1097 (1991).
13. F. T. Ulaby, E. Michielssen, U. Ravaioli, Fundamentals of applied electromagnetics. 73–74 (2016).
14. C. Asci, A. Sadeqi, W. Wang, H. Rezaei Nejad, S. Sonkusale, Design and implementation of magnetically-tunable quad-band filter utilizing split-ring resonators at microwave frequencies. *Sci. Rep. Uk* **10**, 1050 (2020).
15. V. Kaim *et al.*, Ultra-miniature circularly polarized cpw-fed implantable antenna design and its validation for biotelemetry applications. *Sci. Rep. Uk* **10**, 6795 (2020).
16. A. C. Ferrari *et al.*, Science and technology roadmap for graphene, related two-dimensional crystals, and hybrid systems. *Nanoscale* **7**, 4598–4810 (2015).
17. V. K. Guna *et al.*, Plant-based completely biodegradable printed circuit boards. *IEEE T. Electron Dev.* **63**, 4893–4898 (2016).
18. A. K. Awasthi, J. Li, L. Koh, O. A. Ogunseitan, Circular economy and electronic waste. *Nat. Electron.* **2**, 86–89 (2019).
19. X. Yun, Z. Xiong, L. Tu, L. Bai, X. Wang, Hierarchical porous graphene film: An ideal material for laser-carving fabrication of flexible micro-supercapacitors with high specific capacitance. *Carbon* **125**, 308–317 (2017).
20. Y. Liu *et al.*, Rapid roll-to-roll production of graphene films using intensive joule heating. *Carbon* **155**, 462–468 (2019).
21. R. Song *et al.*, Flexible graphite films with high conductivity for radio-frequency antennas. *Carbon* **130**, 164–169 (2018).

22. K. Pan *et al.*, Sustainable production of highly conductive multilayer graphene ink for wireless connectivity and iot applications. *Nat. Commun.* **9**, 5197 (2018).
23. P. K. Nayak, Direct growth of graphene on insulator using liquid precursor via an intermediate nanostructured state carbon nanotube. *Nanoscale Res. Lett.* **14**, 107 (2019).
24. K. Jaakkola, H. Sandberg, M. Lahti, V. Ermolov, Near-field uhf rfid transponder with a screen-printed graphene antenna. *IEEE Trans. Compon. Packag. Manuf. Technol.* **9**, 616–623 (2019).
25. M. Dashti, J. D. Carey, Graphene microstrip patch ultrawide band antennas for thz communications. *Adv. Funct. Mater.* **28**, 1705925 (2018).
26. Y. Wang *et al.*, Reduced graphene oxide film with record-high conductivity and mobility. *Mater. Today* **21**, 186–192 (2018).
27. K. R. Paton *et al.*, Scalable production of large quantities of defect-free few-layer graphene by shear exfoliation in liquids. *Nat. Mater.* **13**, 624–630 (2014).
28. C. Teng *et al.*, Ultrahigh conductive graphene paper based on ball-milling exfoliated graphene. *Adv. Funct. Mater.* **27**, 1700240 (2017).
29. G. Xin *et al.*, Large-area freestanding graphene paper for superior thermal management. *Adv. Mater.* **26**, 4521–4526 (2014).
30. B. Shen, W. Zhai, W. Zheng, Ultrathin flexible graphene film: An excellent thermal conducting material with efficient emi shielding. *Adv. Funct. Mater.* **24**, 4542–4548 (2014).
31. R. Song *et al.*, Sandwiched graphene clad laminate: A binder-free flexible printed circuit board for 5g antenna application. *Adv. Eng. Mater.* **22**, 2000451 (2020).
32. C. Fan *et al.*, Electromagnetic shielding and multi-beam radiation with high conductivity multilayer graphene film. *Carbon* **155**, 506–513 (2019).
33. S. Jiang *et al.*, Millimeter wave phased array antenna based on highly conductive graphene-assembled film for 5g applications. *Carbon* **196**, 493–498 (2022).
34. A. Iqbal *et al.*, Anomalous absorption of electromagnetic waves by 2d transition metal carbonitride ti3cntx (MXene). *Science* **369**, 446 (2020).
35. A. Sarycheva *et al.*, 2d titanium carbide (MXene) for wireless communication. *Sci. Adv.* **4**, u920 (2018).
36. P. He, M. Cao, W. Cao, J. Yuan, Developing MXenes from wireless communication to electromagnetic attenuation. *Nano Micro Lett.* **13**, 115 (2021).
37. T. S. Tran, N. K. Dutta, N. R. Choudhury, Graphene inks for printed flexible electronics: Graphene dispersions, ink formulations, printing techniques and applications. *Adv. Colloid Interfac.* **261**, 41–61 (2018).
38. S. N. H. Sa Don *et al.*, Analysis of graphene antenna properties for 5g applications. *Sensors-Basel* **19**, 4835 (2019).
39. D. Tang *et al.*, Highly sensitive wearable sensor based on a flexible multi-layer graphene film antenna. *Sci. Bull.* **63**, 574–579 (2018).
40. R. Song *et al.*, High-conductive graphene film based antenna array for 5g mobile communications. *Int. J. Rf Microw. C. E.* **29**, e21692 (2019).
41. S. Feng, T. Yao, Y. Lu, Z. Hao, S. Lin, Quasi-industrially produced large-area microscale graphene flakes assembled film with extremely high thermoelectric power factor. *Nano Energy* **58**, 63–68 (2019).
42. Q. Yang *et al.*, Ultrathin graphene-based membrane with precise molecular sieving and ultrafast solvent permeation. *Nat. Mater.* **16**, 1198–1202 (2017).
43. G. Xin *et al.*, Highly thermally conductive and mechanically strong graphene fibers. *Science* **349**, 1083–1087 (2015).
44. L. G. Cançado *et al.*, General equation for the determination of the crystallite size la of nanographite by raman spectroscopy. *Appl. Phys. Lett.* **88**, 163106 (2006).
45. G. Xin *et al.*, Microfluidics-enabled orientation and microstructure control of macroscopic graphene fibres. *Nat. Nanotechnol.* **14**, 168–175 (2019).
46. M. Braunovic, *Electrical Contacts: Fundamentals* (Applications and Technology, 2006).
47. S. Gupta, W. T. Navaraj, L. Lorenzelli, R. Dahiya, Ultra-thin chips for high-performance flexible electronics. *Npj Flex. Electron.* **2**, 1–17 (2018).
48. T. Leng *et al.*, Graphene nanoflakes printed flexible meandered-line dipole antenna on paper substrate for low-cost rfid and sensing applications. *IEEE Antenn. Wirel. Propag. Lett.* **15**, 1565–1568 (2016).
49. X. Li *et al.*, Self-reinforcing graphene coatings on 3d printed elastomers for flexible radio frequency antennas and strain sensors. *Flex. Print. Electron.* **2**, 035001 (2017).
50. M. Akbari *et al.*, Fabrication and characterization of graphene antenna for low-cost and environmentally friendly rfid tags. *IEEE Antenn. Wirel. Propag. Lett.* **15**, 1569–1572 (2016).
51. X. Huang *et al.*, Binder-free highly conductive graphene laminate for low cost printed radio frequency applications. *Appl. Phys. Lett.* **106**, 203105 (2015).
52. W. Wang *et al.*, High-performance printable 2.4 ghz graphene-based antenna using water-transferring technology. *Sci. Technol. Adv. Mater.* **20**, 870–875 (2019).
53. R. Song *et al.*, Wideband and low sidelobe graphene antenna array for 5g applications. *Sci. Bull.* **66**, 103–106 (2020).
54. M. Shahpari, D. V. Thiel, The impact of reduced conductivity on the performance of wire antennas. *IEEE T. Antenn. Propag.* **63**, 4686–4692 (2015).
55. C. A. Balanis, *Antenna Theory: Analysis and Design, Hoboken, NJ* (Wiley, USA, 2016).
56. R. Song *et al.*, A graphene-assembled film based mimo antenna array with high isolation for 5g wireless communication. *Appl. Sci.* **11**, 2382 (2021).
57. A. Barreiro, F. Boerrnert, M. H. Ruemmeli, B. Buechner, L. M. K. Vandersypen, Graphene at high bias: Cracking, layer by layer sublimation, and fusing. *Nano Lett.* **12**, 1873–1878 (2012).
58. A. Akbari *et al.*, Highly ordered and dense thermally conductive graphitic films from a graphene oxide/reduced graphene oxide mixture. *Matter* **2**, 1198–1206 (2020).